RSC Advances

PAPER

View Article Online
View Journal | View Issue

Open Access Article. Published on 05 March 2019. Downloaded on 10/19/2025 12:10:04 PM.
This article is licensed under a Creative Commons Attribution-NonCommercial 3.0 Unported Licence.

Check for updates

Cite this: *RSC Adv.*, 2019, **9**, 7334

# Point defect-reduced colloidal $SnO_2$ electron transport layers for stable and almost hysteresis-free perovskite solar cells†

Yeonkyeong Ju, ‡[a] So Yeon Park, ‡[a] Hyun Soo Han [b] and Hyun Suk Jung *[a]

Received 15th January 2019
Accepted 26th February 2019

DOI: 10.1039/c9ra00366e

rsc.li/rsc-advances

The commercialization of perovskite solar cells has been investigated, but the instability of their light-absorbing layers remains a problem. We demonstrate that the use of colloidal $SnO_2$ nanoparticles prevents perovskite light absorber decomposition, reduces the hysteresis index to 0.1%, and increases the power conversion efficiency to 19.12%.

Perovskite solar cells (PSCs) are suitable for next-generation photovoltaic systems, due to their unique optoelectronic properties and compositional versatility.[1–5] In particular, the solution-based coating process enables the production of low-cost solar modules with high throughput; studies for the commercialization of this process have been conducted, reporting a power conversion efficiency of 23.3%.[6,7] However, the instability (under moist conditions, high temperatures, oxygen, UV light[8–11]) and the hysteresis issue of PSCs have been considered bottlenecks for their commercialization.[12,13] The influence of charge trap sites in electron transport layers (ETLs) has been studied to solve these problems.[12,14,15]

The $TiO_2$ layer is a well-known ETL, which requires high-temperature (>400 °C) heat treatment and has been used to realize high-performance PSCs. However, the $TiO_2$ layer can reduce the long-term stability and amplify the hysteresis phenomenon.[16] $SnO_2$ is one of the most attractive materials for the replacement of $TiO_2$, due to its wide-band gap, high electron mobility, and proper band alignment with the light-absorbing perovskite layer.[17–21] Still, $SnO_2$-based PSCs are affected by hysteresis, defined in terms of hysteresis index (HI = difference between PCEs measured under backward and forward bias/PCE measured under backward bias) > 5%.[17,22–24] To mitigate the hysteresis effect, various preparation methods have been proposed for the $SnO_2$ ETLs.[25] Among them, colloidal $SnO_2$ nanoparticles possessing high crystallinity have been reported as one of the most promising ETL materials for PSCs.[19,26,27] Uniformly coated $SnO_2$ colloid layers have exhibited excellent PCE,[27] but the hysteresis and long-term stability of PSCs based on colloidal $SnO_2$ have not been investigated in detail.

In this work, we successfully fabricated high efficiency perovskite solar cells using ligand-capped colloidal $SnO_2$ nanoparticles; also, we investigated the thermal stability of perovskite light-absorbing layers coated with conventional sol–gel $SnO_2$ and colloidal $SnO_2$ layers. Colloidal $SnO_2$ effectively inhibited both the decomposition of perovskite layers and the hysteresis phenomena in the PSCs, compared to the sol–gel derived $SnO_2$ layers. The maximum power conversion efficiency (PCE) of the PSC based on colloidal $SnO_2$ layers (19.12%) was higher than that of the PSC based on sol–gel derived $SnO_2$ layers (16.45%).

The structural and superficial characteristics of sol–gel $SnO_2$ (S-$SnO_2$) and colloidal $SnO_2$ (C-$SnO_2$) are shown in Fig. S1 (ESI†).

The XRD patterns of S-$SnO_2$, which was prepared at 180 °C, indicated an amorphous structure (Fig. S1a, ESI†), while C-$SnO_2$ was crystallized in a rutile structure (JCPDS card no. 41-1445). Transmittance electron microscopy images and the analysis of reduced fast Fourier transform patterns confirm the crystalline nature of C-$SnO_2$ (Fig. S1b and c, ESI†).

The Fourier-transform infrared spectroscopy (FTIR) spectra in Fig. 1a indicate the abundance of organic groups in C-$SnO_2$. The strong peaks at 2852 and 2924 $cm^{-1}$ are associated with the presence of an organic capping layer. These organic capping layers may annihilate the point defects like oxygen vacancies on the surface of $SnO_2$. Fig. 1b shows the X-ray spectroscopy (XPS) spectra for the O 1s core levels of S-$SnO_2$ and C-$SnO_2$. The relatively high intensity of OH peaks at 531.73 eV for S-$SnO_2$, compared to those for C-$SnO_2$, implies that surface oxygen vacancies were more common in S-$SnO_2$ than in C-$SnO_2$.[28,29] Surface oxygen vacancies in oxide materials are known for being passivated by OH groups.[29] Also, they have been reported to work as surface charge trap sites in oxide ETLs, interfering with the electron transport between perovskite and ETLs.[30] The Sn 3d XPS peaks (Fig. 1c) for S-$SnO_2$ are shifted towards lower binding energy than those for C-$SnO_2$, indicating an abundance of oxygen vacancies in S-$SnO_2$. A lower number of oxygen vacancies in C-$SnO_2$ might be ascribed to the passivation effect of organic capping layers.[31,32]

[a]*School of Advanced Materials Science & Engineering, Sungkyunkwan University, Suwon 16419, Republic of Korea. E-mail: hsjung1@skku.edu*

[b]*Department of Mechanical Engineering, Stanford University, Stanford, USA*

† Electronic supplementary information (ESI) available. See DOI: 10.1039/c9ra00366e

‡ These authors contributed equally.



This journal is © The Royal Society of Chemistry 2019

Open Access Article. Published on 05 March 2019. Downloaded on 10/19/2025 12:10:04 PM.
This article is licensed under a Creative Commons Attribution-NonCommercial 3.0 Unported Licence.

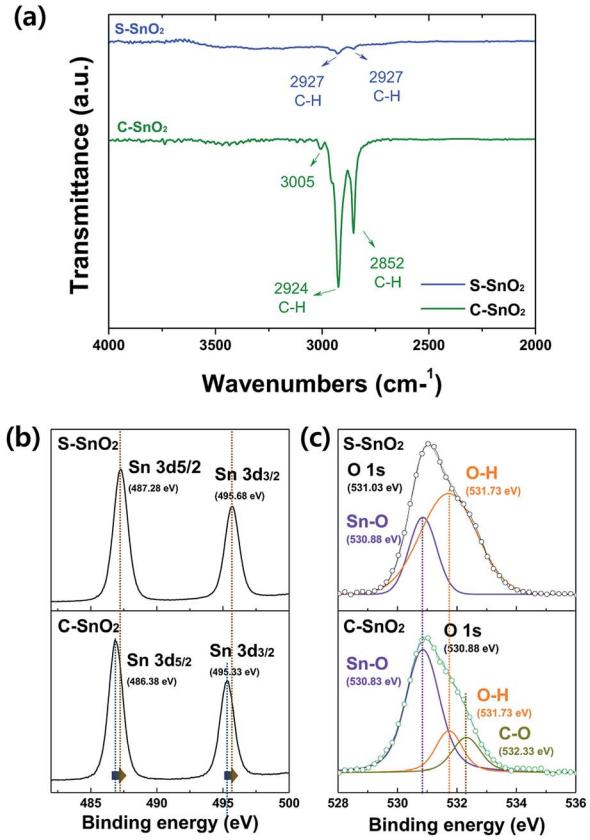


Fig. 1 (a) FT-IR spectra for the S-$SnO_2$ and C-$SnO_2$ films, between 4000 and 2000 $cm^{-1}$; (b) XPS spectra of S-$SnO_2$ and C-$SnO_2$ films at O 1s core level, and (c) at Sn 3d core level.

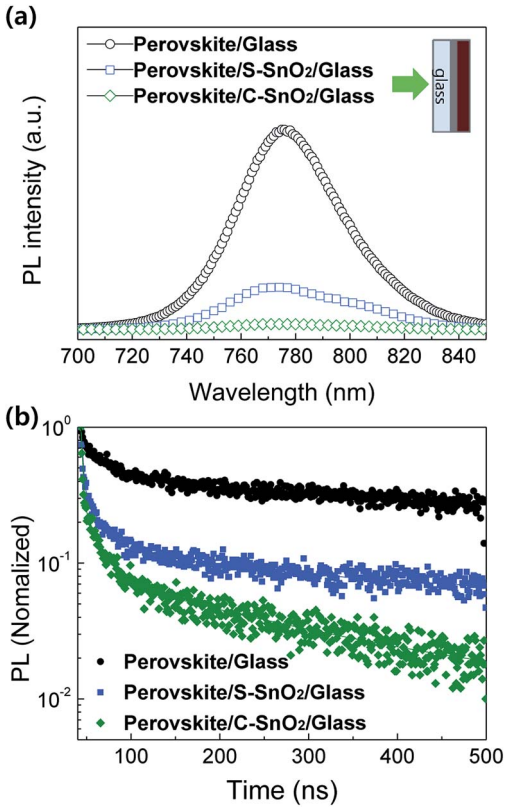


Fig. 2 (a) Photoluminescence (PL) spectra and (b) time-resolved photoluminescence (TRPL) curves of perovskite/glass, perovskite/S-$SnO_2$/glass and perovskite/C-$SnO_2$/glass.

The photoluminescence (PL) spectra for perovskite/glass, perovskite/S-$SnO_2$/glass, and perovskite/C-$SnO_2$/glass are plotted in Fig. 2a. The C-$SnO_2$-based sample exhibits lower PL intensities (770 nm) compared with the S-$SnO_2$-based sample; this indicates an improved quenching effect for the perovskite/C-$SnO_2$ interface, due to the facilitated electron extraction properties of C-$SnO_2$. Time-resolved photoluminescence (TRPL) curves (Fig. 2b) show consistent relationships with steady-state PL. The presence of less oxygen vacancies in C-$SnO_2$ allows a rapid extraction of electrons from the light-absorbing perovskite layer, reducing the electron–hole recombination.[33]

Fig. 3a shows the thermal degradation behavior of the perovskite light-absorbing layers coated on S-$SnO_2$ and C-$SnO_2$ layers, at an annealing temperature of 100 °C in ambient air with relative humidity of approximately 25–30%. The perovskite light-absorbing layer on S-$SnO_2$ was decomposed (and changed color) earlier, while the C-$SnO_2$ layer exhibited relatively retarded decomposition behavior. The UV-vis spectra support the retarded decomposition behavior of perovskite light-absorbing layers on C-$SnO_2$, compared with those on S-$SnO_2$ (Fig. 3b and c). Moreover, the change in XRD patterns (Fig. 3d and e) is consistent with the UV-vis spectra for perovskite layers on S-$SnO_2$ and C-$SnO_2$. The perovskite (110) peak at 14.2° for the perovskite light-absorbing layers on S-$SnO_2$, completely disappeared in 24 hours annealing-time. In contrast, the (110) peak for the perovskite on C-$SnO_2$ lasted for over 60 hours annealing time. In real solar cell devices, C-$SnO_2$-based perovskite cells exhibit much better stability. The long-term stability under light-soaking conditions was estimated under AM 1.5G in ambient air. After 100 minutes of light soaking, the C-$SnO_2$-based device retained 90%, whereas the S-$SnO_2$-based device retained only 60% of the initial PCE (Fig. 3f). Under dark conditions, the C-$SnO_2$-based cell exhibited excellent stability: it maintained 95% of the initial efficiency after one month. The results are shown in detail Fig. S2a and b (ESI†). At the surface of $SnO_2$ crystals, the oxygen vacancies form hydroxyl groups to passivate these point defects by bonding with the hydrogen atom of water.[34,35] These hydroxyl groups themselves may facilitate the degradation of perovskite layer. The degradation of the perovskite film in C-$SnO_2$ case can be slowed down by reducing the surface hydroxyl groups correspondent with the reduced point defects. Moreover, the improved long-term stability of the C-$SnO_2$-based cell can be ascribed to enhanced electron extraction from the perovskite layer to the C-$SnO_2$, resulting from a low number of oxygen vacancies, which can work as charge traps. Such charge traps in oxide ETL have been known for assisting the decomposition of perovskite materials with $H_2O$ and/or $O_2$ under illuminated conditions.[30]

The C-$SnO_2$-based cell was almost hysteresis-free (Fig. 3g): the PCEs obtained from the reverse and forward scans were 18.34% and 18.17%, respectively; the resultant HI was 0.1%. On the other hand, for the S-$SnO_2$-based cell the PCEs from the reverse and forward scans were 16.46% and 13.69% (Fig. 3g and h),

Open Access Article. Published on 05 March 2019. Downloaded on 10/19/2025 12:10:04 PM.
This article is licensed under a Creative Commons Attribution-NonCommercial 3.0 Unported Licence.

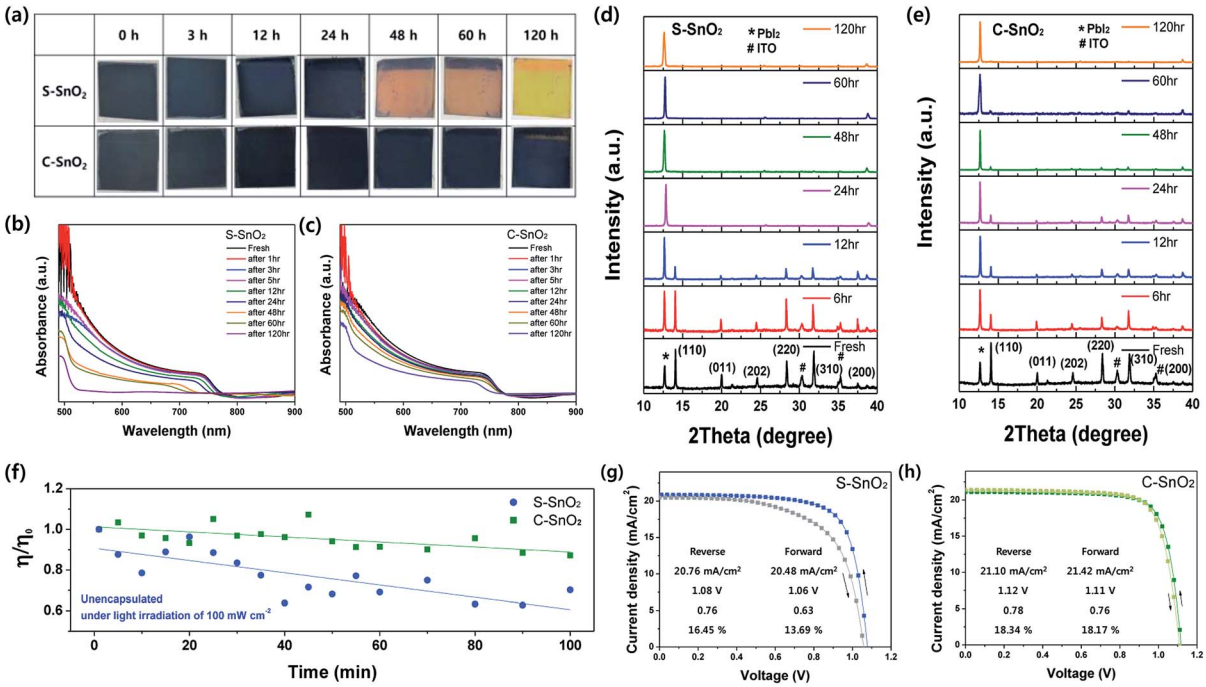


Fig. 3 (a) Degradation behavior of perovskite light-absorbing layers on S-$SnO_2$ and C-$SnO_2$; (b) UV-vis absorbance spectra of perovskite light-absorbing layers on S-$SnO_2$ and (c) C-$SnO_2$; (d) XRD patterns of perovskite light-absorbing layers on S-$SnO_2$ and (e) C-$SnO_2$ as a function of the thermal annealing times at 100 °C. (f) Change in the efficiencies of S-$SnO_2$ and C-$SnO_2$-based cells without encapsulation, under constant AM 1.5G illumination in below 20% humidity and 25 °C ambient air; (g) $J$–$V$ curves of devices based on S-$SnO_2$ and (h) C-$SnO_2$ measured with reverse and forward scans.

respectively; the resultant HI was 11.72%. The absence of hysteresis in the C-$SnO_2$-based cell can be explained by a facilitated electron extraction, linked to a low concentration of oxygen vacancies.[36] The average photovoltaic parameters of C-$SnO_2$- and S-$SnO_2$-based PSCs are presented in Fig. S3a–d (ESI†). The C-$SnO_2$-based cell exhibits a higher average efficiency (18.34%) than the S-$SnO_2$-based cell (16.45%). This higher efficiency results from the higher an open circuit voltage ($V_{oc}$) of 1. 12 V and fill factor (FF) of 0.78 of the C-$SnO_2$-based cell, compared to those of the S-$SnO_2$-based cell (1.08 V and 0.76, respectively). The lower $V_{oc}$ and FF values of the S-$SnO_2$-based cell are related to facilitated electron extraction, as already suggested by our PL analyses. The $J_{sc}$, $V_{oc}$, and FF of the maximum PCE cell, based on C-$SnO_2$, were 21.11 mA $cm^{-2}$, 1.14 V, and 0.79, respectively; the corresponding yielding PCE was 19.12% (Fig. S3e, ESI†). The series resistance ($R_s$) and the shunt resistance ($R_{sh}$) were also estimated from the $J$–$V$ curves. The corresponding detailed device parameters are summarized in Table S1 (ESI†). The C-$SnO_2$-based on PSCs shows a notably higher $R_{sh}$ of 33.18 kΩ $cm^2$ compared with S-$SnO_2$-based on PSCs, as well as the lower $R_s$ of 29.10 Ω $cm^2$ caused by enhanced charge extraction. The external quantum efficiency (EQE) of the device is represented in Fig. S4a (ESI†), where the integrated photocurrent of 21.24 mA $cm^{-2}$ is close to that of the $J$–$V$ curves. The steady-state PCE of the device was also measured to be 16.92% under a constant bias voltage of 0.80 V (Fig. S4b, ESI†).

Besides the reduced oxygen vacancies, other factors such as energy band structure and electrical conductivity for each ETL may influence the charge extraction. In our previous study, the conduction band minimum ($E_{CB}$) was reported as 4.11 eV and 4.09 eV for S-$SnO_2$ and C-$SnO_2$, respectively. The energy barrier for electron transfer from perovskite to C-$SnO_2$ ETLs was found to decrease, resulting in the enhanced performance.[27] Also, electrical conductivities of each ETLs were measured. As shown in Fig. S5 (ESI†), the higher conductivity of C-$SnO_2$ ETL also causes the reduced hysteresis and better PCE.[37] Our study demonstrates that C-$SnO_2$ with reduced oxygen vacancies can be used successfully as an ETL material, allowing the production of highly efficient, long-term stable, and hysteresis-free PSCs.

In summary, we demonstrated that C-$SnO_2$ ETLs improve the stability of PSCs and eliminate any associated hysteresis effect. The structural and surface properties of C-$SnO_2$ revealed its crystalline structure and the occurrence of additional low surface point defects, including oxygen vacancies, compared to the more conventional S-$SnO_2$. The C-$SnO_2$-based PSC showed excellent stability and almost zero hysteresis (HI = 0.1%) compared to the S-$SnO_2$-based PSC (HI = 11.72%). Our PL analyses demonstrated the excellent quenching characteristics of C-$SnO_2$, which result from facilitated electron extraction (due to the low amount of oxygen vacancies). Moreover, the C-$SnO_2$-based PSC showed a relatively high efficiency (19.12%). These C-$SnO_2$ nanoparticles with high crystallinity and low oxygen vacancy are promising electron transport materials; hence, they can be used to produce PSCs with excellent photovoltaic performances: high efficiency, long-term stability, and free of hysteresis effects.

Open Access Article. Published on 05 March 2019. Downloaded on 10/19/2025 12:10:04 PM.
This article is licensed under a Creative Commons Attribution-NonCommercial 3.0 Unported Licence.

## Conflicts of interest

The authors of this manuscript have no conflicts of interest.

## Acknowledgements

This research was supported by the National Research Foundation of Korea (NRF), grant funded by the Korea government (NRF-2017R1A2B3010927, 2015M1A2A2056827, 2018M3C1B7021994 and 2018M1A2A2058207).

## Notes and references

1 M. Grätzel, *Nat. Mater.*, 2014, **13**, 838.
2 A. Kojima, K. Teshima, Y. Shirai and T. Miyasaka, *J. Am. Chem. Soc.*, 2009, **131**, 6050–6051.
3 S. D. Stranks, G. E. Eperon, G. Grancini, C. Menelaou, M. J. Alcocer, T. Leijtens, L. M. Herz, A. Petrozza and H. J. Snaith, *Science*, 2013, **342**, 341–344.
4 G. Xing, N. Mathews, S. Sun, S. S. Lim, Y. M. Lam, M. Grätzel, S. Mhaisalkar and T. C. Sum, *Science*, 2013, **342**, 344–347.
5 W. S. Yang, B.-W. Park, E. H. Jung, N. J. Jeon, Y. C. Kim, D. U. Lee, S. S. Shin, J. Seo, E. K. Kim and J. H. Noh, *Science*, 2017, **356**, 1376–1379.
6 H. J. Snaith, *J. Phys. Chem. Lett.*, 2013, **4**, 3623–3630.
7 J. You, Z. Hong, Y. Yang, Q. Chen, M. Cai, T.-B. Song, C.-C. Chen, S. Lu, Y. Liu and H. Zhou, *ACS Nano*, 2014, **8**, 1674–1680.
8 G. Abdelmageed, L. Jewell, K. Hellier, L. Seymour, B. Luo, F. Bridges, J. Z. Zhang and S. Carter, *Appl. Phys. Lett.*, 2016, **109**, 233905.
9 G. Niu, X. Guo and L. Wang, *J. Mater. Chem. A*, 2015, **3**, 8970–8980.
10 J. Yang, B. D. Siempelkamp, D. Liu and T. L. Kelly, *ACS Nano*, 2015, **9**, 1955–1963.
11 H. Zhou, Q. Chen, G. Li, S. Luo, T.-b. Song, H.-S. Duan, Z. Hong, J. You, Y. Liu and Y. Yang, *Science*, 2014, **345**, 542–546.
12 J. Cao, B. Wu, R. Chen, Y. Wu, Y. Hui, B. W. Mao and N. Zheng, *Adv. Mater.*, 2018, **30**, 1705596.
13 J. Luo, J. Xia, H. Yang, L. Chen, Z. Wan, F. Han, H. A. Malik, X. Zhu and C. Jia, *Energy Environ. Sci.*, 2018, **11**, 2035–2045.
14 F. Giordano, A. Abate, J. P. C. Baena, M. Saliba, T. Matsui, S. H. Im, S. M. Zakeeruddin, M. K. Nazeeruddin, A. Hagfeldt and M. Graetzel, *Nat. Commun.*, 2016, **7**, 10379.
15 M. M. Byranvand, T. Kim, S. Song, G. Kang, S. U. Ryu and T. Park, *Adv. Energy Mater.*, 2018, **8**, 1702235.
16 J. Ma, G. Yang, M. Qin, X. Zheng, H. Lei, C. Chen, Z. Chen, Y. Guo, H. Han and X. Zhao, *Adv. Sci.*, 2017, **4**, 1700031.
17 J. P. C. Baena, L. Steier, W. Tress, M. Saliba, S. Neutzner, T. Matsui, F. Giordano, T. J. Jacobsson, A. R. S. Kandada and S. M. Zakeeruddin, *Energy Environ. Sci.*, 2015, **8**, 2928–2934.
18 Q. Dong, Y. Shi, C. Zhang, Y. Wu and L. Wang, *Nano Energy*, 2017, **40**, 336–344.
19 Q. Jiang, L. Zhang, H. Wang, X. Yang, J. Meng, H. Liu, Z. Yin, J. Wu, X. Zhang and J. You, *Nat. Energy*, 2017, **2**, 16177.
20 W. Ke, D. Zhao, A. J. Cimaroli, C. R. Grice, P. Qin, Q. Liu, L. Xiong, Y. Yan and G. Fang, *J. Mater. Chem. A*, 2015, **3**, 24163–24168.
21 C. Xiao, C. Wang, W. Ke, B. P. Gorman, J. Ye, C.-S. Jiang, Y. Yan and M. M. Al-Jassim, *ACS Appl. Mater. Interfaces*, 2017, **9**, 38373–38380.
22 E. H. Anaraki, A. Kermanpur, L. Steier, K. Domanski, T. Matsui, W. Tress, M. Saliba, A. Abate, M. Grätzel and A. Hagfeldt, *Energy Environ. Sci.*, 2016, **9**, 3128–3134.
23 Q. Jiang, Z. Chu, P. Wang, X. Yang, H. Liu, Y. Wang, Z. Yin, J. Wu, X. Zhang and J. You, *Adv. Mater.*, 2017, **29**, 1703852.
24 M. Zhu, W. Liu, W. Ke, S. Clark, E. B. Secor, T.-B. Song, M. G. Kanatzidis, X. Li and M. C. Hersam, *J. Mater. Chem. A*, 2017, **5**, 24110–24115.
25 D. Yang, R. Yang, K. Wang, C. Wu, X. Zhu, J. Feng, X. Ren, G. Fang, S. Priya and S. F. Liu, *Nat. Commun.*, 2018, **9**, 3239.
26 Z. Zhu, Y. Bai, X. Liu, C.-C. Chueh, S. Yang and A. K.-Y. Jen, *Adv. Mater.*, 2016, **28**, 6478–6484.
27 S. Y. Park, M. Y. Baek, Y. Ju, D. H. Kim, C. S. Moon, J. H. Noh and H. S. Jung, *J. Phys. Chem. Lett.*, 2018, **9**, 5460–5467.
28 X. Zhang, J. Qin, Y. Xue, P. Yu, B. Zhang, L. Wang and R. Liu, *Sci. Rep.*, 2014, **4**, 4596.
29 P. Wang, J. Zhao, J. Liu, L. Wei, Z. Liu, L. Guan and G. Cao, *J. Power Sources*, 2017, **339**, 51–60.
30 N. Ahn, K. Kwak, M. S. Jang, H. Yoon, B. Y. Lee, J.-K. Lee, P. V. Pikhitsa, J. Byun and M. Choi, *Nat. Commun.*, 2016, **7**, 13422.
31 S. Bai, Y. Jin, X. Liang, Z. Ye, Z. Wu, B. Sun, Z. Ma, Z. Tang, J. Wang and U. Würfel, *Adv. Energy Mater.*, 2015, **5**, 1401606.
32 B. Luo, S. B. Naghadeh, A. L. Allen, X. Li and J. Z. Zhang, *Adv. Funct. Mater.*, 2017, **27**, 1604018.
33 F. Ali, N. D. Pham, H. J. Bradford, N. Khoshsirat, K. Ostrikov, J. M. Bell, H. Wang and T. Tesfamichael, *ChemSusChem*, 2018, **11**, 3096–3103.
34 M. F. Mohamad Noh, N. A. Arzaee, J. Safaei, N. A. Mohamed, H. P. Kim, A. R. Mohd Yusoff, J. Jang and M. A. Mat Teridi, *J. Alloys Compd.*, 2019, **773**, 997–1008.
35 A. Senocrate, T. Acartürk, G. Y. Kim, R. Merkle, U. Starke, M. Grätzel and J. Maier, *J. Mater. Chem. A*, 2018, **6**, 10847–10855.
36 B. Chen, M. Yang, X. Zheng, C. Wu, W. Li, Y. Yan, J. Bisquert, G. Garcia-Belmonte, K. Zhu and S. Priya, *J. Phys. Chem. Lett.*, 2015, **6**, 4693–4700.
37 M. Park, J.-Y. Kim, H. J. Son, C.-H. Lee, S. S. Jang and M. J. Ko, *Nano Energy*, 2016, **26**, 208–215.